Energy Advances

ROYAL SOCIETY OF CHEMISTRY

PAPER

View Article Online
View Journal | View Issue

Cite this: *Energy Adv.*, 2022, 1, 344

Improvement on the electrochemical performance by morphology control of nanostructured $La_{0.6}Sr_{0.4}CoO_{3-\delta}$-$Gd_{0.1}Ce_{0.9}O_{1.95}$ cathodes for IT-SOFC†

Leandro Marcelo Acuña, *[ab] Marcelo Daniel Cabezas[a] and Rodolfo Oscar Fuentes [bc]

Received 9th November 2021,
Accepted 19th April 2022

DOI: 10.1039/d2ya00085g

rsc.li/energy-advances

The effect of the particle's shape of $Gd_{0.1}Ce_{0.9}O_{2-d}$ (GDC) nanopowders on the electrochemical performance of $La_{0.6}Sr_{0.4}CoO_{3-\delta}$ (LSC)–GDC composite cathodes was experimentally studied by electrochemical impedance spectroscopy (EIS). Composites were made of nanostructured LSC perovskite (average crystallite size D = 30 nm) mixed with nanostructured GDC powder (D = 8 nm) of irregular particle shape or with spherical particles of 200 nm diameter. Symmetrical cells (cathode/electrolyte/cathode) with different weight ratios of LSC:GDC (100 : 0, 75 : 25, 50 : 50 and 25 : 75 wt%) thick cathodes were fabricated by the screen-printing method and tested by EIS in the temperature range of 500–700 °C under a synthetic air flow of 100 mL min^{-1}. These nanostructured composite materials exhibited excellent performance (area-specific resistance – ASR – values in the range of 0.019–0.032 Ω cm^2 for an operating temperature of 700 °C). The best performance was achieved at a weight ratio of 75 : 25 wt% (LSC : GDC) when nanostructured GDC spheres were employed. This enhanced performance can be attributed to GDC morphology along with GDC anionic conduction, which prevent the blocking of LSC electrochemical reaction sites on surface, keeping them active by depleting its surface of adsorbed and reduced oxygen. The limiting processes were determined to take place on the LSC surface. New insight on cobalt's speciation under working-like conditions, determined by *in situ* X-ray Absorption Spectroscopy (XAS) experiments, suggests that the ease of cobalt atoms for changing their oxidation state is the key feature that rules the electrochemical activity of LSC and an atomistic model that explains it is proposed.

Introduction

The solid oxide fuel cells (SOFCs) are energy conversion devices that convert the chemical energy of fuels (hydrogen, natural gas, and other hydrocarbons) directly into electrical energy with high efficiency and low emission of pollutants.[1] However, at the high working temperature of SOFCs (800–1000 °C), several undesirable effects, such as further chemical reaction and diffusion, which affects the materials' structure, take place and reduce the SOFC's lifespan and performance. So, there is great interest in developing new materials for intermediate-temperature SOFC (IT-SOFC) devices, which can be operated between 500 and 700 °C.[2] In particular, materials with perovskite structure have long been investigated due to their excellent mixed ionic and electronic conduction (MIEC) properties, which make them suitable for application as electrodes in IT-SOFCs. $La_{0.6}Sr_{0.4}CoO_{3-\delta}$ is one of most the promising cathode materials for IT-SOFCs due to its significantly high ionic conductivity and surface exchange kinetics, along with excellent electronic conduction.[3–5]

Nanostructured materials have attracted attention due to the size dependence of the crystallographic parameters and electronic structure that may favour its physical and electrochemical properties.[6–8] One of the common goals of many researchers is to prepare nanostructured electrodes with high surface area and controlled morphology. The nanostructured cathodes prepared by different methods have significantly increased surface area for the oxygen surface exchange reaction. In order to evaluate the effect of cathode morphology on the oxygen reduction reaction (ORR) performance, cathodes based in LSC nanotubes with different diameters were reported by Sacanell *et al.* and Bellino *et al.*[9,10] The resulting ASR was significantly higher at 600 °C (1–2 Ω cm^2) than that for

[a] *Department of Functional Advanced Materials, UNIDEF, V. Lopez, B1603ALO Buenos Aires, Argentina. E-mail: lacuna@citedef.gob.ar*
[b] *CONICET, C1033AAJ Buenos Aires, Argentina*
[c] *INN, Department of Physics, CAC-CNEA, Gral. San Martín, B1650LWP Buenos Aires, Argentina*

† Electronic supplementary information (ESI) available: XANES procedure and analysis, XRD, EIS and SEM analysis. See DOI: https://doi.org/10.1039/d2ya00085g

nanostructured LSC powders reported by Acuña *et al.* (0.395 Ω cm^2).[7]

Dieterle *et al.* reported an ORR with ASR of 0.023 Ω cm^2 at 600 °C where a dip coating technique was employed to obtain nano-porous LSC thin films with the thickness in the range of 150–200 nm.[11] The use of the thin-film deposition method is promising but there are several issues such as optimization of the electrode microstructure, substrate choice and component durability that need to be addressed before commercialization.[12–14] One successful strategy to improve chemical stability of LSC thin films is to deposit several LSC/GDC bilayers with a thickness of tens of nm on a substrate of $NdGaO_3$ by pulsed laser deposition (PLD).[15]

The presence of the solid electrolyte phase in the porous cathode should serve to enhance the thermomechanical compatibility of the electrode with the electrolyte by improving the adhesion and matching the thermal expansion coefficient (TEC) of the materials.[16] Thus, composite cathodes are generally favoured over single-phase MIECs. In particular, $Gd_{0.1}Ce_{0.9}O_{1.95}$ is considered to be one of the best electrolytes for IT SOFC applications,[17] and it is known by its low reactivity with LSC, what made the LSC–GDC composite cathode extensively investigated.[16,18–23] Moreover, GDC layers are employed to prevent chemical reaction and ion migration between LSC and YSZ or SSZ (Ytria or Scandia-Stabilized Zirconia, respectively) electrolytes.[16,18,24] It is assumed that improved ionic diffusion and additional triple phase boundary (TPB) reaction lead to performance enhancement, but it is still not clear how cathode performance can be correlated with microstructure characteristics for the LSC–GDC composite cathode. In addition, there is no consensus about the processes and reactions that take place in the cathode and different models were proposed.[25] This difficulty is based on the lack of information, coming from direct probes at atomic scale, on the chemical properties of cobalt atoms in LSC under working-like conditions of IT-SOFCs. The knowledge of the "oxygen diffusion mechanisms at an atomic scale is of vital importance" for the development of strategies for improving IT-SOFC performance.[26]

The use of indirect methods, such as neutron diffraction, X-ray diffraction or iodometric or coulometric titration, led to the conclusion that cobalt atom plays a secondary and passive role in LSC electrochemical activity and to identify vacancies as the main feature behind the electrochemical activity of LSC material.[27–29] The last type of experiments is known by its high accuracy, but it only provides the average oxidation state of a sample. In addition, it is a destructive experiment and do not allow for reproducing special environment conditions as those found in SOFC's electrodes.

XAS experiments, comprising XANES and EXAFS regions (Near Edge and Extended X-ray Absorption spectrum, respectively), are direct probes for the chemical and local order properties of a selected element in a material, they are not destructive and can be performed under controlled environment conditions. Previous studies,[13,30–34] were not able to analyse cobalt's speciation in LSC because of the lack of proper Co(IV) standard. Some of them studied the sample only at room temperature. In all cases, they made qualitative analyses, such as comparing the XANES profile of Co-K edge in LSC with some reference standards or following the Co-K edge energy shift as function of strontium content, sample's temperature or oxygen partial pressure. Those qualitative analyses only gave, in the best cases, the average oxidation state (near +3) of cobalt atom, leading to the same conclusion found in the others works that used indirect methods, namely, that the electrochemical activity of LSC (and also changes in the electronic and spin configuration of Co atoms) can be explained only by vacancy formation and crystal structure distortions, such as octahedron's tilting of oxygen atoms or phase transitions. "Most of the studies of LSC, however, did not discuss the correlations among MIEC, crystal structure parameters, electron densities, band structures, and spin configurations, quantitatively."[35] Some works that focused the attention on the spin state properties at low or room temperature, made assumptions on cobalt's oxidation state from oxygen vacancy concentration or changes in the pre-edge-energy region of the Co-K edge XANES.[31–33]

On the other hand, Takeda *et al.* stated that the electrochemical activity of LSC (adsorption, diffusion, dissociation and reduction of oxygen and delivering of oxygen anions to the electrolyte phase, GDC, for instance) would partially rest on the ability of Co atoms for changing their oxidation state according to environment conditions and the electrochemical potential in a cell.[36] Experimental evidence of this was observed by Acuña *et al.*[8] In this last approach, it was observed that Co atoms easily change their oxidation state in nanostructured LSC powders in response to increasing temperature from 20 to 500 °C under air flow. In the same way, Baskar and Adler pointed out the strong dependence of electron transport properties in LSC with spin states and oxidation states, which clearly justifies the use of XANES to address these issues.[37] Finally, the lack of detailed fundamental studies of the chemical properties of active materials at the atomic scale has prevented breaking the performance limits through the rational development of advanced materials.

Therefore, in this study, the effect of the particle's shape of GDC nanostructured powders on the electrochemical performance of LSC–GDC composite cathodes were studied on symmetrical cells (cathode/electrolyte/cathode) by varying the relative content of nanostructured LSC (D = 30 nm) and nanostructured GDC powders (D = 8 nm) of irregular (standard) particle shape or spherical particle shape of 200 nm diameter. The analysis of EIS data (recorded in the temperature range of 500–700 °C) showed an enhanced performance of the composite made of spherical particles of GDC and that the observed improvement takes place in the LSC phase. EIS analysis also suggests that the rate limiting processes take place on LSC surface. In order to analyse the LSC activity at atomic scale, *in situ* XAS experiments were performed on LSC nanopowders under working-like conditions of IT-SOFC's cathodes. Novel information about cobalt speciation gave new insight on the chemical activity of cobalt atom in LSC, and a model at the atomic scale that describes the path of oxygen anions in the composite cathode is proposed. Additionally, we found evidence that, once the oxygen vacancies in the LSC reaches a maximum concentration, disproportionation reaction in cobalt atoms is

triggered, possibly acting as a stabilizing mechanism that prevents nanostructured LSC from phase instability.

XANES analysis also offers a possible explanation on how GDC particle's shape can contribute to improve LSC performance. We offer in this work a hypothetical mechanism that integrates the results coming from every experiment performed in this study, by which GDC particle shape can contribute to this factual enhancement of LSC performance. Nevertheless, experiments contributing with conclusive evidence of the relationship between GDC particle shape and LSC performance are out of the boundaries of the present study. Despite this, we believe that the results presented in this work will encourage future defining works on this issue.

Experimental

In order to obtain different morphologies of nanostructured $Gd_{0.1}Ce_{0.9}O_{1.95}$ solid solutions, two chemical methods, previously reported by the authors, were employed: cation complexation (CC) and microwave assisted hydrothermal homogeneous co-precipitation (MW).[38,39] Nanostructured GDC powders obtained by CC method will be denoted as GDC_{CC} and those obtained by MW, as GDC_{MW}.

Synthesis of nanostructured GDC_{CC} powders

$Ce(NO_3)_3{\cdot}6H_2O$ (99.99%, Alfa Aesar) and $Gd(NO_3)_3{\cdot}6H_2O$ (99.9%, Alfa Aesar) were employed as precursors. Each nitrate was dissolved in deionized H_2O separately and then the solutions were mixed to obtain nitrate solutions with molar ratios of Ce:Gd appropriate for the preparation of products. Citric acid (99.5%, Merck) was dissolved in d.i. water and this was added to the cation nitrate solution in appropriate amounts to give a molar ratio of final total oxide to citric acid of 1 : 2. After homogenization of this solution, the temperature was raised to 80 °C, and the solution maintained under stirring to remove excess water and to convert it to a transparent gel. While raising the temperature, the solution became more viscous with evolution of foam, and finally it gelled without any visible precipitation or turbidity. During the dwell at 80 °C there was an increase in viscosity and simultaneous elimination of water and NO_x. The initial thermal decomposition of the precursor was carried out at 250 °C for 1 H in air and the resulting ash-like material was calcined at 500 °C for 1 H in air.

Synthesis of spherical particles of nanostructured GDC

$Ce(NO_3)_3{\cdot}6H_2O$ (99.99%, Alfa Aesar) and $Gd(NO_3)_3{\cdot}6H_2O$ (99.9%, Alfa Aesar) were employed as precursors. Each nitrate was dissolved in pure deionized H_2O separately and then the solutions were mixed to obtain a 0.1 M nitrate solution with molar ratios of Ce:Gd and Ce:Pr appropriate for the preparation of GDC and PrDC, respectively. Urea was added in order to give a molar ratio of urea:final oxide of 4 : 1 and 60 ml of the resulting solution was placed in a Teflon lined autoclave. A Milestone ETHOS 1 Advanced Microwave Digestion system was employed. The sealed autoclave was placed in the oven and was heated to 120 °C with a ramp rate of 30 °C min^{-1} – with oven power set to 550 W – and then kept at this temperature for 1 h. After cooling, the white powder product was collected by centrifugation (2.5 min at 7830 rpm) and dried at 37 °C for 12 H. After calcination at 500 °C in air for 1 H, the nanostructured GDC spheres were obtained.[39]

Synthesis of nanostructured LSC powders

LSC nanopowders were synthesized by the gel-combustion (GC) method, starting from $Sr(NO_3)_2$ (Aldrich, 99%), $La(NO_3)_3{\cdot}6H_2O$ (Aldrich, 99.999%) and $Co(NO_3)_2{\cdot}6H_2O$ (Aldrich, >98%) as precursors. Glycine ($C_2H_5O_2N$) (Merck, ≥99%) was used as the complexing agent and the fuel for the combustion step.[8]

Synthesis of Co(III) and Co(IV) standards

$LaCoO_3$ was synthesized from $La(NO_3)_3{\cdot}6H_2O$ (Aldrich, 99.999%) and $Co(NO_3)_2{\cdot}6H_2O$ (Aldrich, >98%) precursors and citric acid (Aldrich, 99%) following the procedure described by Taguchi *et al.*[40] $BaCoO_3$ was synthesized using $Ba(NO_3)_2$ (Sigma-Aldrich, 99.999%) and $Co(NO_3)_2.6H_2O$ following the procedure described by Milt *et al.*[41] Commercial CoO (Sigma-Aldrich, ≥99.99%) was employed as Co(II) reference material.

Preparation of symmetrical cell for EIS

Slurries of nanostructured LSC–GDC composite cathodes with different weight ratios of LSC:GDC (100 : 0, 75 : 25, 50 : 50 and 25 : 75 wt%)and DECOFLUX vehicle were prepared using a weight ratio powder:vehicle close to 3 : 1, pursuing a viscosity similar to that exhibited by commercial paints. As an example of the nomenclature used in this work, cathode composite with a 75 wt% of nanostructured LSC powder and 25 wt% of nanostructured GDC_{CC} or GDC_{MW} powder will be denoted as $LSC75–GDC_{CC}25$ or $LSC75–GDC_{MW}25$, respectively.

Dense electrolytes of 1 mm thick and 10 mm diameter were obtained from commercial $Sm_{0.2}Ce_{0.8}O_{1.9}$ powder (SDC, NexTech Materials) uniaxially pressed under 20 kPa and then sintered in a tubular furnace at 1400 °C for 5 H. Thick films of area 0.24 cm^2 and thickness of near 75 μm were then screen printed onto both faces of the SDC electrolytes and fired in a range of temperatures between 800 °C and 950 °C for 2 H. As LSC phase is an excellent electronic conductor in the range of temperatures of interest for this study, no other current collector was used (such as Pt paste), as LSC itself acts as current collector.[42] This approach has the advantage of eliminate any possible contribution of the current collector phase to the EIS spectra or any interaction between the noble metal and the cathode phase itself that could modify the electrode performance.

Characterization of LSC–GDC cathodes

X-ray powder diffraction (XPD) was employed for preliminary structural characterization using a Philips PW 3710 diffractometer with Cu K-α radiation at room temperature (RT). Scans were collected in the range of 2θ = 20–80° with steps of 0.02° and step counting time of 4 s.

The morphology of nanostructured LSC–GDC cathodes was studied with a scanning electron microscope SEM FEI Quanta 200.

Electrochemical measurements

Electrochemical properties of LSC–GDC cathodes were studied by EIS using the symmetrical cell configuration, cathode/electrolyte/cathode. EIS measurements were carried out using an Autolab PGSTAT302N instrument (Metrohm, Echo Chemie) in the temperature range of 500–700 °C under a synthetic air flow and 10 and 5% O_2/N_2 flow (100 ml min^{-1}). The symmetric cells were excited with a sine wave of 20–50 mV amplitude in the frequency range of 0.1 Hz to 1 MHz sampling ten points per decade on a log scale. The EIS spectra were fitted by means of the equivalent circuit method using the ZView 2 software (Version 3.0, Scribner Associates, Inc.). The fittings were performed in the confidence range for this equipment, at frequencies below 30 kHz, according to manufacturer's recommendation and the quality of experimental data.

X-ray absorption measurements

X-ray Absorption Near Edge Structure (XANES) experiments were carried out at the D08B-XAFS2 beam line of the Brazilian Synchrotron National Laboratory (LNLS), Brazil, in transmission mode.[43] The energy was selected with a Si(111) monochromator. 8 mg of LSC, $LaCoO_3$, $BaCoO_3$ and CoO powders were mixed with 92 mg of boron nitride and uniaxially pressed applying 0.2 kg m^{-2} to a 13 mm diameter die. The pellets were placed in an iron sample holder and introduced in the tubular quartz chamber of a furnace with refrigerated Kapton™ (DuPont) windows. Experiments were performed under synthetic air flow and 5% O_2/N_2 flow (50 ml min^{-1}). The entrance and exit of the gas flow were at the ends of the tube. Samples were heated from room temperature to 700 °C at a rate of 10 °C min^{-1} and a stabilization time of 10 min. XAS spectra of Co-K edge were measured from 6900 to 8700 eV. Energy step of 0.3 eV and counting time of 4 s was used for the XANES region. The data reduction was done following the standard procedure[8,44] using WinXAS 3.1 software.[45] A detailed description of the procedure can be found in the ESI's XANES section.

No XAS experiments we carried out on LSC–GDC mixtures because the XAS signal of Gd-L_2 (with edge energy E_0 = 7898 eV), that lies within the energy range of the EXAFS signal of Co-K edge, and the EXAFS oscillations of Gd-L_3 edge (E_0 = 7211 eV), may complicate the XANES analysis of the Co-K edge. In addition, self-absorption in LSC–GDC powders considerably diminishes XAS signal of the Co-K edge (between 30 and 70% of signal loss). The XANES of Sr-K and La-L_3 edges were not measured because no relevant information for this study was expected, as these cations exhibit only one oxidation state (+2 and +3, respectively).

Results and discussion

In this section is analyzed the effect of GDC particle's morphology on the electrochemical activity of LSC–GDC composite cathodes and a model describing reactions that involve molecular and atomic oxygen on the cathode's surface will be developed, based on the chemical properties of cobalt atoms in LSC. The effect that the morphology of LSC particles (nanopowders of irregular shape, nanotubes of different diameters, nanowires and others) may have on the electrochemical performance of LSC–GDC composite cathodes is a very interesting question that deserves to be developed in another work, due to the amount of data that it is needed to be analyzed and the different issues to be discussed.

Morphological and structural characterization

The thickness of the porous thick electrodes was approximately 75 μm in every case. The microstructure of the electrode layer is highly porous and the interface between the electrode and the electrolyte shows good contact between these two layers (Fig. 1 and 2). LSC75–GDC_{CC}25 cathode consists of particles with two distinct particle size. The larger ones, in the scale of the μm can be ascribed to the LSC phase, which are partially covered with smaller ones that can be related to the GDC phase (Fig. 1 and Fig. S4, ESI†).

LSC75–GDC_{MW}25 cathode is made of two types of particles with well differentiated particle shapes: particles of irregular shape with particle size on the order of the μm, ascribable to LSC, and spherical particles of about 200 nm diameter, corresponding to GDC_{MW} (Fig. 2 and Fig. S4, S5, ESI†). From now on, we will refer to the latter simply as GDC_{MW} spheres, in opposition to GDC_{CC} nanopowder. At high magnifications it is possible to observe GDC_{MW} particles of spherical shape (Fig. 2b and c) embedded in the LSC powder. Some trend to agglomeration in GDC spheres is observed and may play an important role in composite cathode's performance.

All the reflections observed in the XRD patterns of LSC–GDC cathodes correspond to the LSC (rhombohedral phase: $R\bar{3}c$ space group, No. 167,) or to the GDC phase (cubic phase: $Fm\bar{3}m$ space group) and no reaction or segregated phases are observed neither in the fresh cathodes (Fig. 3) nor in the LSC75–GDC_{MW}25 cathode after the long term stability test (Fig. S6,

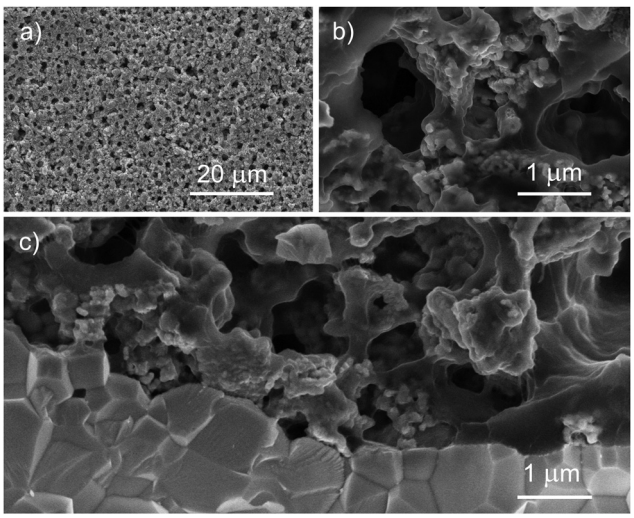

Fig. 1 SEM micrographs of LSC75–GD_{CC}C25 cathode. (a) Top view at low magnification. (b) Detail of top view. (c) Cross section with SDC electrolyte at the bottom. The smallest particles in the cathode belong to the GDC phase.

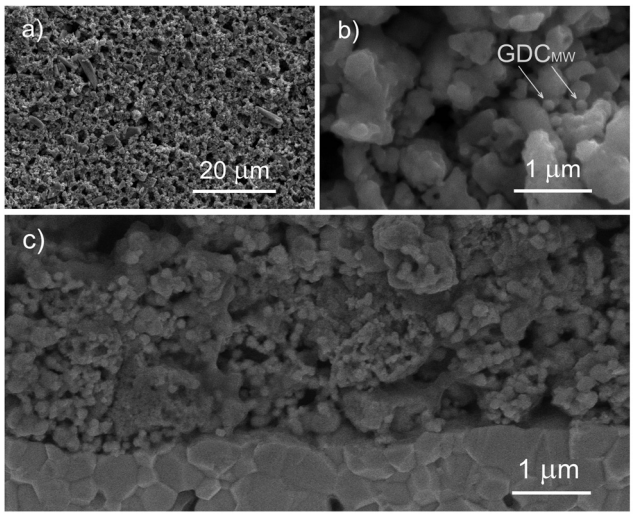

Fig. 2 SEM micrographs of LSC75–GD_{MW}25 cathode. (a) Top view (low magnification). (b) Detail of top view. Arrows spot GDC spheres. (c) Cross section including SDC electrolyte. Largest cathode's particles belong to LSC phase.

ESI†). Detailed Rietveld refinement results are listed in Tables S1 and S2 (ESI†). The lattice parameters obtained by means of the Rietveld refinement method are in excellent agreement with reference data found in the literature (Tables S3 and S4, ESI†). The exception is the work of Gwon *et al.* (later reproduced in the review of Jun *et al.*), who studied the $La_{1-x}Sr_xCoO_{3-\delta}$ phases as function of Sr content x.[46,47] While Gwon *et al.* reported that the cubic phase is present at room temperature in the $La_{1-x}Sr_xCoO_{3-\delta}$ samples with low Sr content ($x \leq 0.4$), Petrov *et al.* and Closset *et al.*, among others, have identified at room temperature the rhombohedral phase for $0 \leq x < 0.6$ and the cubic phase for $0.6 \leq x \leq 1$.[3,31,48,49]

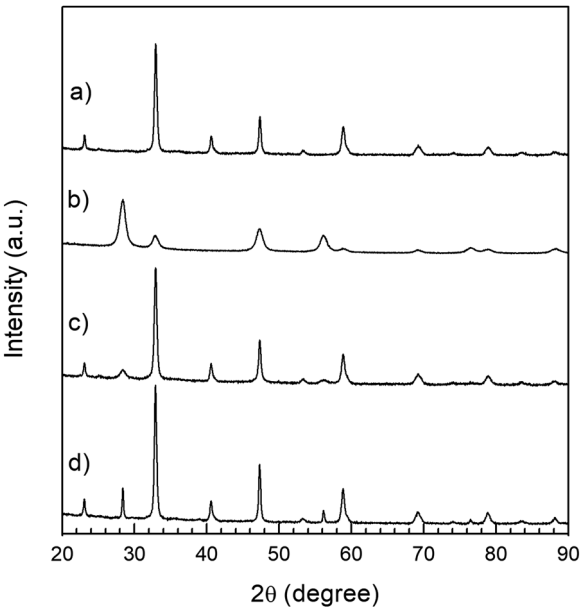

Fig. 3 XRD patterns. (a) LSC nanopowders; (b) GDC powder with particles of spherical shape; (c) LSC75–GDC_{MW}25 cathode before the sintering process; (d) LSC75–GDC_{MW}25 cathode after 2H at 850 °C.

EIS studies

Electrochemical impedance spectra were measured in the temperature range of 500–700 °C for the half-cells constructed from LSC–GDC cathodes with various LSC:GDC weights and different sintering temperatures. Every Nyquist plot exhibits two distinct arcs, and the Bode phase plots, two well resolved peaks (Fig. 4). The plots of polarization area specific resistance (ASR_{pol}) as function of sintering temperature show that the lowest value of ASR_{pol} is obtained for LSC75–GDC25, LSC50–GDC50 and LSC25–GDC75 sintered at 850, 875 and 925 °C, respectively (Fig. S7, ESI†). The best performance is achieved with a GDC load of 25 wt% (powder or spheres). This is in agreement with several works dedicated to LSC–GDC composites, that obtained the best results with the 30 wt% GDC load (among 20, 30, 40 wt% GDC).[18,20,21] Nevertheless, Kim and Shikazono, in a combined theoretical and experimental work, reported that the lowest polarization resistance is achieved with a 70 wt% GDC load.[50]

EIS spectra were fitted with different equivalent circuit models. Fig. 5a shows a scheme of the equivalent circuit that will be discussed here, while Fig. 5b and c are examples corresponding to LSC75–GDC_{CC}25 sample at 700 °C under synthetic air flow along with the fitting curve and the contribution of each circuit element.

Between 600 and 700 °C the electrolyte contribution to the EIS spectra is pure resistive and it was fitted to the $R1$ resistance (Fig. 5a). The inductance contribution of the wires was modelled with a parallel $L_2//R_2$ (L_2 in the order of 10^{-7} H and $R_2 \approx 1.9\ \Omega$). The high frequency (HF) and low frequency (LF) arcs where represented with two parallel R//CPE. A middle frequency (MF) circuit was also used to improve the fit to EIS spectra in LSC and LSC75–GDC_{CC}25 cathodes. It was tested an R//CPE and a Finite Length Warburg-short (W_S) elements with similar quality of fit.[51–53] The use of either model didn't affect the values obtained for the parameters of other circuit elements. Here we present the results obtained for the W_S element and the reason for this will become apparent in the course of the discussion of the results.

Examination of Arrhenius plot indicates that LSC75–GDC_{MW}25 exhibits the lowest polarization losses in the whole

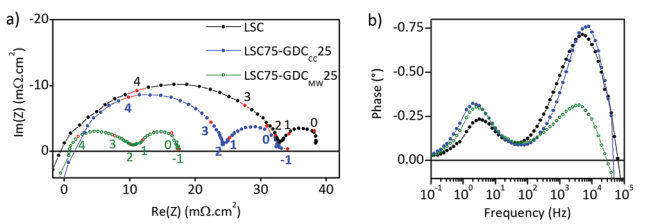

Fig. 4 (a) Nyquist plot of normalized EIS spectra and (b) bode-phase plot for LSC, LSC75–GDC_{CC}25 and LSC75–GD_{MW}25 cathodes at 700 °C under synthetic air flow. Inserted numbers close to red data points are their log(frequency) value. In (a), the pure resistive contribution of the electrolyte was subtracted from the data for easy comparison.

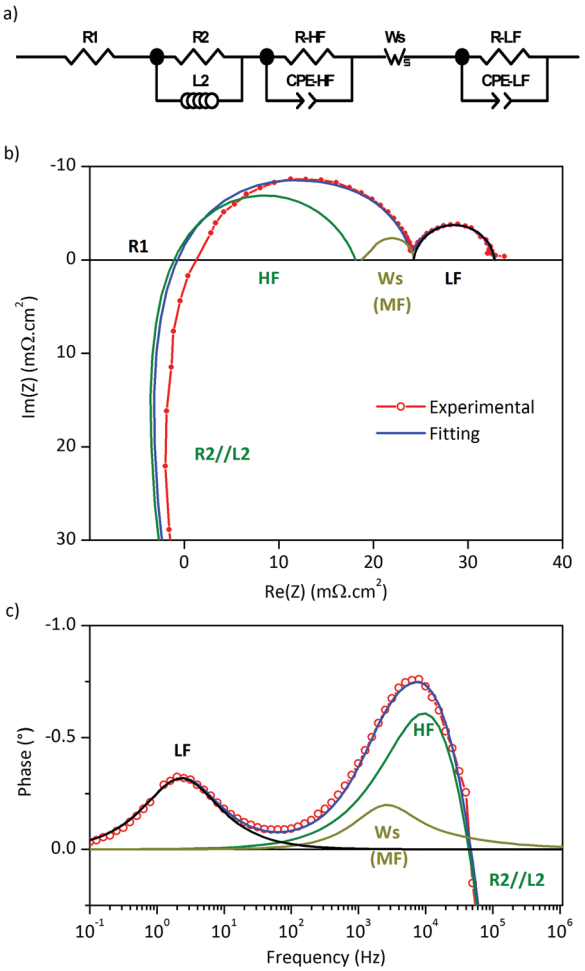

Fig. 5 Equivalent circuit analysis of EIS spectrum of LSC75–$GDC_{CC}25$ cathode at 700 °C under synthetic air flow. (a) Scheme of the equivalent circuit used to fit the spectrum. (b) Normalized Nyquist plot and (c) bode phase diagrams of the experimental data along with the fitting function. In (b) and (c) it is also included the contribution of each circuit element to the fitting curve. In (b) the contribution of R_1 element was subtracted from the experimental data and fitting function.

temperature range (Fig. 6a), where $ASR_{TOTAL} = ASR_{HF} + ASR_{MF} + ASR_{LF}$. The analysis of each contribution points out that the improvement is related to the processes represented by the HF and MF arcs (Fig. 6b and c, respectively). In fact, ASR_{MF} in LSC75–$GDC_{MW}25$ is negligible (Table 1).

The W_S contribution in LSC (Fig. 6c) is truncated at temperatures below 625 °C, due to the decreasing weight that the W_S element has on the overall ASR with decreasing temperature. As consequence, the statistical error on the related parameters W_R (Warburg resistance) and W_T (Warburg characteristic time) is higher at lower temperatures. Therefore, we chose to focus our analysis at T = 700 °C. At this temperature, every arc is resolved more easily and, in consequence, results are more reliable. Within LSC-based thick cathodes, the ASR_{TOTAL} values achieved in this work are among the best reported in literature to the best of our knowledge (Table S5, ESI†).

The W_S contribution to the total ASR of LSC–GDC_{CC} is very low at high temperatures but, at 500 °C, it became comparable

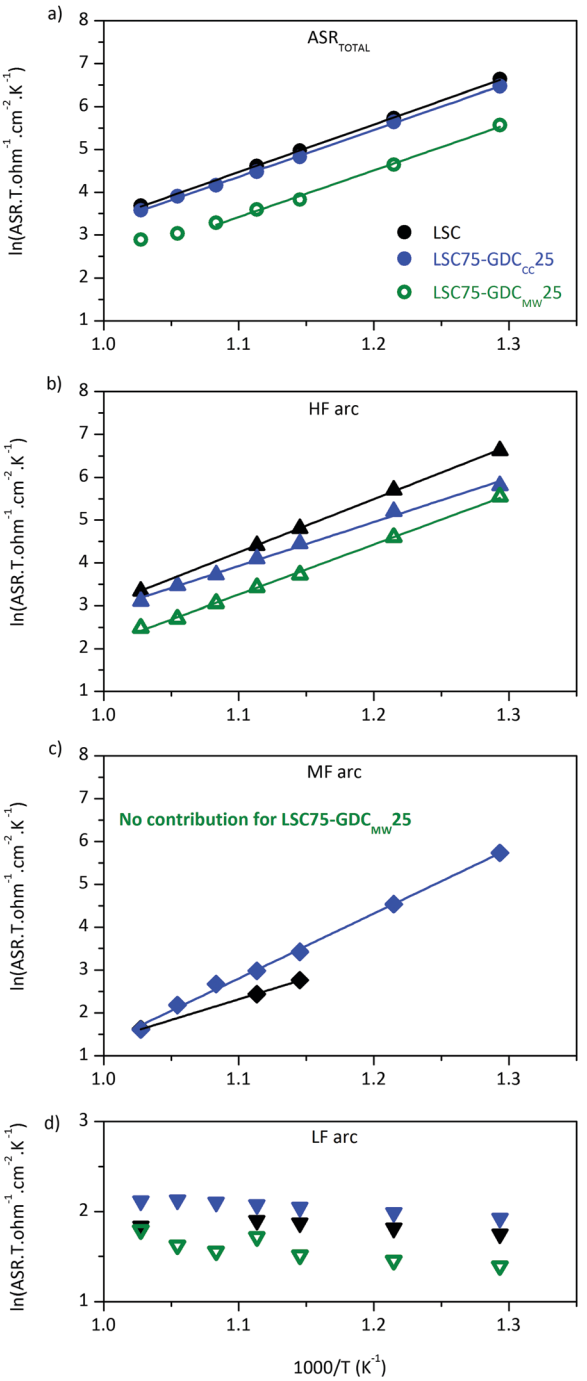

Fig. 6 Comparison of the electrochemical performance of LSC, LSC75–$GDC_{CC}25$ and LSC75–$GD_{MW}25$ cathodes between 500 and 700 °C. Arrhenius plots for (a) ASR_{TOTAL}; (b) ASR_{HF}; (c) ASR_{MF} and (d) ASR_{LF}. The colours correspondence to each sample is inserted in panel (a). Straight lines are the linear regression for the experimental data. Dashed line in panel (a) represents the extrapolation of the linear regression and spots the departure of the experimental data from the straight line at $T > 650$ °C.

to that of the HF arc (Fig. 6b and c) of the same sample. This fact is in opposition to the trend observed in the case of LSC cathode. The total E_a (calculated from the analysis of Fig. 6) is in good agreement with Hjalmarsson *et al* (Table 2).[31] The

Table 1 Total polarization resistance and contributions from different processes

	ASR at T = 700 °C (mΩ cm^2)			
Cathode	Total	HF	MF	LF
LSC	41(2)	29.2(1)	5.2(8)	6.4(1)
LSC–GDC$_{CC}$	39(1)	24.7(7)	5.5(8)	8.6(1)
LSC–GDC$_{MW}$	18.6(2)	12.4(1)	—	6.2(1)

origin of the different activation energy of each arc will be discussed later in this section.

The low frequency arc proved to be weak dependent on temperature (Fig. 6d). As the temperature decreases, it gets more difficult to resolve this LF arc from the HF or MF arcs. This is the reason why we chose to fix R_{LF} to the value obtained from the fit to the spectra at 700 °C in air for LSC and LSC–GDC$_{CC}$. This weak dependency on temperature makes its relative contribution more important as ASR$_{HF}$ and ASR$_{MF}$ decreases with increasing temperature. This is the reason why the Arrhenius plot of the ASR$_{TOTAL}$ of LSC75–GDC$_{MW}$25 departs from the straight line above 650 °C (Fig. 6a). Above this temperature, the HF and LF arcs become comparable.

Several works found in the literature have stated a relationship between the value of n (the slope of the linear function that fits the plot of log(1/ASR) as function of the logarithm of the oxygen partial pressure, log(P_{o2})), and specific processes in cathodes (Table 3 and Fig. S8, ESI†). According to Takeda *et al*,[36] the HF process (that exhibits $n \approx 0.25$ in every case) would be related to Langmuir's type oxygen atom adsorption, where there is a very low fraction of adsorption sites occupied by O atoms. This reaction is represented by the equation:

$$O_{ad} + 2e' + V_O^{\bullet\bullet} \leftrightarrow O_O^{\times} \quad (1)$$

which means that this limiting process consists in a charge transfer process on the surface. Here, O_{ad} is an oxygen atom adsorbed in surface and $O_O^{\times}$ is the oxygen anion in a normal lattice site. Although the E_a of the HF process is lower in the LSC75–GDC$_{CC}$25 sample, the ASR$_{HF}$ value is lower in the LSC75–GDC$_{MW}$25 sample between 500–700 °C. This result would be related to a better electrical connectivity between grains, as will be discussed later.

On the other side, the low frequency arc in Fig. 5b exhibits a simple inverse law ($n \approx 1$) as function of P_{o_2}. Always according to Takeda, this corresponds to a reaction in which molecular oxygen is involved in this rate limiting process, which consists

Table 2 Activation energy of the electrodes and of the high and middle frequency arc

	E_a (eV)		
Cathode	Total	HF	MF
LSC	0.96(1)	1.07(1)	0.83(1)
LSC–GDC$_{CC}$	0.94(1)	0.88(4)	1.30(3)
LSC–GDC$_{MW}$	0.94(3)	1.01(2)	—

Table 3 Analysis of the slope (n) of ASR^{-1} as function of P_{o2}

	Slope of log(1/ASR) *vs.* log(P_{o_2}) at T = 700 °C		
Cathode	HF	MF	LF
LSC	0.25(1)	0.52(7)	1.3(1)
LSC–GDC$_{CC}$	0.25(7)	0.32(3)	1.15(3)
LSC–GDC$_{MW}$	0.18(8)	0.9[a]	1.18(5)

[a] Estimated.

of three steps described by the equations:

$$O_2(g) \leftrightarrow O_{2,ad}$$
$$O_{2,ad} \leftrightarrow O_{2,ad,ers} \quad (2)$$
$$O_{2,ad,ers} \leftrightarrow 2O_{ad,ers}$$

where $O_{2,ad,ers}$ and $O_{ad,ers}$ is an oxygen molecule or atom adsorbed at the electrochemical reaction site (ers), respectively.[36] As the LF arc proved to be weakly dependent on temperature, it is possible that the rate limiting process associated to this arc consists in molecular oxygen adsorption and diffusion, without the contribution of a dissociative adsorption step.

The process that contributes to the middle frequency arc is more difficult to analyse because of its low ASR value (close to 15% of the total ASR at 700 °C in air) and its high associated uncertainty. Its dependency with P_{o_2} in LSC cathode is n = 0.5. This is in accordance with an atomic oxygen diffusion and reduction process, described by[36]

$$O_{2,ad,ers} \leftrightarrow 2O_{ad,ers}$$
$$2O_{ad} \leftrightarrow 2O_{ad,ers} \quad (3)$$
$$O_{ad,ers} + 2e' + V_O^{\bullet\bullet} \leftrightarrow O_O^{\times}$$

Eqn (3) shows that the process can consist of three steps: (1) dissociation of adsorbed O_2; (2) diffusion of O atoms to *ers*; and (3) CT process. The analysis suggests that the CT process is present in both HF and MF arcs. This is possible because the HF arc is related to Langmuir's type oxygen absorption and the MF arc to oxygen adsorption with diffusion steps, and each process exhibits a different characteristic time.

The lower value of n = 0.32 calculated for the LSC75–GDC$_{CC}$25 cathode (Fig. S8b, ESI†) and the higher value of n = 0.9 for LSC75–GDC$_{MW}$25 cathode would indicate that the weight of each step in eqn (3) is different in them. We can see in eqn (3) that the first step describes the same reaction observed in the last step of eqn (2). On the other hand, the last step in eqn (3) consists in the same reaction described by eqn (1). So, it is possible that n = 0.32 is indicating that the CT step in eqn (3) is the major contributor to the ASR$_{MF}$ in LSC75–GDC$_{CC}$25. Following the same reasoning, n = 0.9 would be indicating that the two last reactions in eqn (3) have a lower weight than the first one, the dissociation of adsorbed O_2.

These results would indicate that the ad-atomic diffusion process has more active paths in the composite than in the LSC cathode. Maybe, the diffusion path to the electrochemical

reaction sites is shorter (or faster) in the composites. This, along with a lower contribution of the adsorbed O_2 dissociation (1st) step in eqn (3) to the ASR_{MF} of LSC75–GDC_{CC}25, makes the whole process more similar to that described in eqn (1) (involving a Langmuir's type oxygen atom adsorption). This hypothesis is consistent with the values obtained for the diffusion characteristic time, W_S–T, in LSC (4.3×10^{-4} s) and in LSC75–GDC_{CC}25 (1.5×10^{-4} s) cathodes. Another possibility is related to the fact that the ionic conduction in GDC at 700 °C is high compared to that exhibited by LSC perovskite,[54] suggesting that the GDC phase is a possible path for oxide ions. This would contribute to deplete the LSC surface of oxygen species, maintaining in this way the electrochemical reaction sites active. This is more apparent in LSC75–GDC_{MW}25 cathode, where the contribution of this middle frequency arc is negligible at 20% O_2/N_2. The value it would take under these conditions is represented by the extended line that fits the experimental data in Fig. S8b (ESI†). The extrapolated ASR value is 0.81 mΩ cm^2, which is relatively very low if it is compared to the other contributions and explains the difficulty of including the W_S element in the fitting of the data under these conditions. This result, along with its lower ASR_{TOTAL} (Table 1), means that the LSC75–GDC_{MW}25 cathode has more active sites on its surface compared to the other film.

The higher value of n = 0.9 for the MF arc of LSC75–GDC_{MW}25 (Fig. S8b, ESI†), along with its lower ASR_{MF} and the lower ASR_{TOTAL}, may rest on the possibility that the combination of GDC_{MW} spheres with LSC powder optimizes the connectivity between the two phases and also improves the percolation of GDC spheres, resulting in faster CT reaction in eqn (3). This is also consistent with the lower ASR values of the HF arc that this cathode exhibits (Fig. 6b).

Factually, the only difference between the two cathodes is the shape of GDC particles. Therefore, the origin of the improvement in LSC–GDC composites is possibly related to the spherical morphology of GDC_{MW}. In fact, the area of the contact surface between one LSC particle and one GDC_{MW} sphere is smaller than that between two particles LSC–LSC or LSC–GDC_{CC}. This has at least two positive aspects. One, GDC_{MW} spheres would prevent that two LSC particles be in contact and sinter during the sintering procedure. In that way, they would keep available more superficial area for reaction (eqn (1)–(3)). This picture is consistent with the differences exhibited by each cathode in the values of the ASR_{LF}. They would suggest that a greater LSC surface is covered by GDC_{CC} powder than by LSC itself or GDC_{MW} spheres. But it has to be mentioned that the variations observed in ASR_{LF} are small enough to be conclusive. The other, already mentioned, is that the GDC phase would contribute to deplete the LSC surface of oxygen anions, keeping low the number of occupied active sites with oxygen species. We will explain this issue in detail after discussing XANES results.

Finally, in order to check the stability of LSC75–GDC_{MW}25 cathode, EIS spectra were recorded at 700 °C after several dwell-times. The experimental data was analysed using the equivalent circuit shown in Fig. 5a. After 101 H at 700 °C in air, ASR_{TOTAL} of LSC75–GDC_{MW}25 cathode showed an increment of 30%, due to the growth of the HF arc (Fig. 7 and Fig. S9, ESI†). The LF arc, associated to diffusion of adsorbed O_2 molecules, remained essentially unchanged, suggesting that no sintering process took place during the test. The small contribution of the MF arc became noticeable and was fit to the W_S element (W_R = 1.1(1) mohm cm^2), and it was constant with time. The increment in the HF arc was observed during the very first hours of the experiment, remaining without any noticeable change for the next 70 hours, in accordance with Tao *et al.*[18] The increment observed in ASR_{TOTAL} and ASR_W at the end of the test (Fig. 7) is more likely to be due to the fall of 0.8 °C in sample's temperature. All these evidences point to loss of efficiency in the CT process, probably due to a small surface reaction between LSC and GDC phases or to element segregation in the surface of the particles.[18] This was not possible to detect by means of XRD analysis. Also, it was observed a small shift in the HF pure resistance R_1 towards higher values (ΔR_1 = 3 mohm cm^2, what represents 0.5% of its initial value of 639 mohm cm^2, or 12% of the initial ASR_{TOTAL}), probably due to the same causes.

XANES of Co-K edge

In this section we offer new insight on cobalt's speciation in LSC powders. The sensibility of Co atoms to changes in P_{O_2} was studied by linear combination fitting (LCF) of Co(II,III,IV) experimental standards to cobalt's XANES spectra in LSC (Fig. S1, ESI†).[8]

XANES experiments showed that the average oxidation state of Co atoms decreases from +3.4 to +3.0 as temperature increases from 20 to 700 °C in air, starting with a mixture of 60% Co^{3+} and 40% Co^{4+} (Fig. 8a and b). This result is in agreement with indirect calculations made by others researchers through, for example, iodometric titration experiments.[27,31] For the first time, it was observed that the Co speciation then gradually evolves to approximately 25% Co^{2+} and Co^{4+} and 50% Co^{3+} with increasing temperature in air. This balance is modified to 17% Co^{2+} and Co^{4+} and 66% Co^{3+} when P_{O_2} decreases to 5% O_2/N_2 at 700 °C.

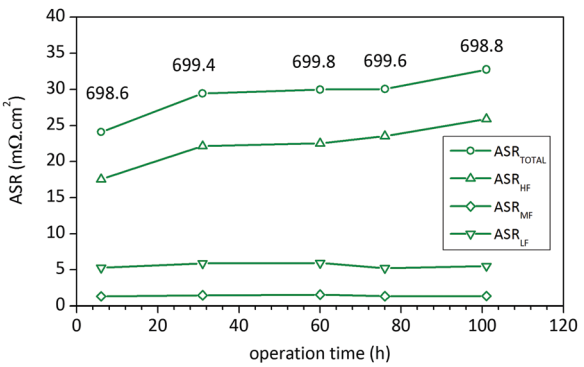

Fig. 7 Long-term operation test of LSC75–GD_{MW}25 cathode at 700 °C during 101 h under synthetic air flow. The evolution of each component with time shows the origin of the increment in ASR_{TOTAL} observed during the first hours of operation. The inserted numbers indicate the temperature of the sample in °C when the measurement was performed.

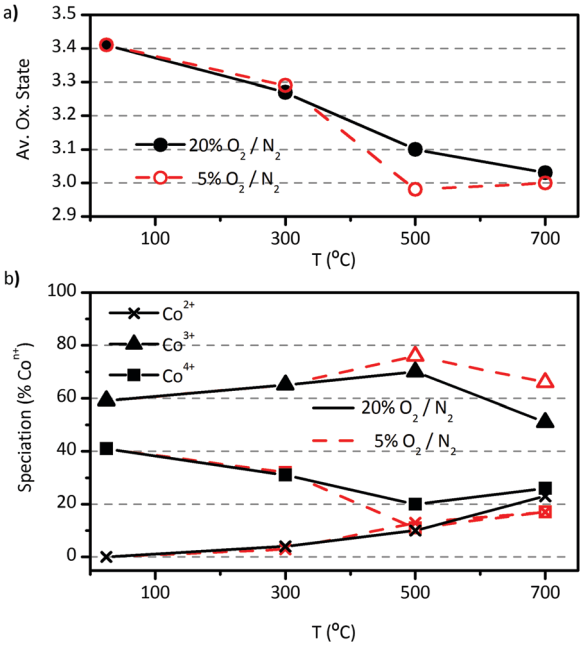

Fig. 8 Analysis of cobalt's oxidation state in LSC nanopowders as function of temperature and under different O_2 concentration in the O_2/N_2 atmosphere. (a) Average oxidation state, and (b) speciation of cobalt atoms in LSC according to Co-K edge XANES analysis using the LCF method.

The average oxidation state of Co (Fig. 8a), calculated from the cobalt's speciation, is in good agreement whit previous works found in the literature.[27,31,35] In addition, the initial amount of 40% Co^{4+} exactly compensates the 40% of Sr^{2+} cations in the A-site, what leads to the conclusion that no vacancies are present in the fresh LSC powder at room temperature. Mineshigue *et al.* have found metal-like behaviour in $La_{1-x}Sr_xCoO_{3-\delta}$ ($x \geq 0.3$ and $\delta = 0$) in the temperature range of 20–1200 °C when no oxygen vacancies are found in the lattice.[55,56] On the other hand, when $x = 0.3$ and $\delta \geq 0.06$ they observed insulator-like behaviour at low temperatures (below 200 °C). Mineshigue *et al.* related the oxidation of Co^{3+} to Co^{4+} (as response to Sr^{2+} doping), to electronic conductivity by means of the creation of holes in the electronic band of Co atoms. In the same way, the loss of Co^{4+} with increasing temperature (Fig. 8b) is in accordance with the metallic-like behaviour.[31]

The low intensity peak between 7709 and 7712 eV in Co K-edge XANES spectra contains information about the electronic configuration and spin state of cobalt atoms and it is originated in the electronic excitation from Co-1s to Co-3d orbitals. This forbidden transition is possible due to the hybridization between the Co-3d and O-2p orbitals, though some researchers have found evidence for quadrupolar transition nature.[33,35,57,58] In any case, it is clear that its features are closely related to the electronic conductivity properties of LSC and that it is strongly affected by the crystal field.[58,59] The reader is invited to consult the ESI,† for a more detailed discussion about this topic. It is worth to mention that the detailed analysis of this peak regarding the electronic conductivity of LSC is beyond the scope of the present study.

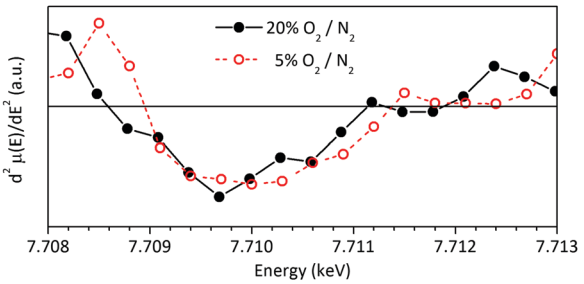

Fig. 9 Analysis of the low intensity peak at $E < E_0$ in the Co-K edge XANES of LSC at 700 °C under synthetic air and 5% O_2/N_2.

The differences observed between both XANES spectra of LSC (Fig. 9) would be related to desorption of O_2.[60] On going from 20 to 5% O_2/N_2, the slight shift towards higher energies and the disappearance of the weak peak at 7712 eV would be associated to the mentioned loss of oxygen in LSC bulk or surface with decreasing P_{O_2} as, in this case, the hybridization between Co 3d and O 2p orbitals also decreases.[59,61,62] This is because when these orbitals are hybridized a charge transfer from Co 3d to O 2p orbitals takes place, creating empty states of lower energy in the hybridized Co 3d orbitals. A very detailed and complementary analysis of this peak can be found in the work of Itoh *et al.*[35]

One final consideration regarding the results in Fig. 8 is that, as temperature increases and O^{2-} vacancies are created, the system seems to evolve to a speciation in which Co^{4+} is exactly compensated by Co^{2+} at 700 °C in air (Fig. 8b). Even though the growth rate followed by the population of each species leaves open the possibility that Co^{2+} overcomes the population of Co^{4+}, an examination of the evolution under low oxygen content shows that, once both species are balanced, they continue in that way at higher temperatures. This result may point out some kind of thermodynamical equilibrium in which, once reached, the disproportionation reaction rules the evolution of the speciation. The analysis suggests that this change of behaviour would be triggered by an upper limit for O^{2-} vacancy concentration in the lattice (Fig. 8a and b). This hypothesis is based on the fact that cobalt's average oxidation state remains essentially constant once it reaches the value of +3 under low oxygen content, while speciation continues evolving by means of the disproportionation reaction. The limit for oxygen vacancy concentration was determined by Petrov *et al.* in microstructured $La_{0.7}Sr_{0.3}CoO_{3-\delta}$,[48] They found a value of $\delta = 0.2$ at 1160 °C and $P_{O_2} \approx 0.01$ beyond which, the sample decomposes. The limit $\delta = 0.2$ is the same that our results suggest. The lower temperature (500 °C) and higher P_{O_2} (0.05) at which we observed it in our sample may be due to its smaller grain and crystallite size. These results point out the outstanding feature nanostructured LSC has, namely, once nanostructured LSC reaches the maximum oxygen vacancy concentration, it uses the disproportionation reaction as a mechanism to keep stabilized the perovskite phase against decomposition. To the best of our knowledge, this is the first time that this mechanism is observed. In addition, the reaction $2Co^{3+} \rightarrow Co^{2+} + Co^{4+}$ would

help to improve the electrical conductivity by increasing the Co^{4+} concentration, as suggested by Mineshigue *et al.*[55,59] This last hypothesis would be very interesting to test. Our results are also in agreement with Abbate *el al.*, who have seen no disproportionation reaction below 360 °C in $LaCoO_3$.[58]

This experiment was intended to have an approach to the behaviour of cobalt atoms in LSC under oxygen demanding conditions (such as in the electrode/electrolyte interface in a SOFC with high oxygen vacancy concentration on the electrolyte side) or under oxygen excess conditions (such as on the electrode/gas interface). The experimental results show that Co atoms in LSC are very sensitive to changes in oxygen concentration in the gas in contact with the LSC particle's surface. This property can be extrapolated to the case of LSC particles in LSC–GDC composite cathodes. Under these conditions, LSC particles are in contact with other particles of LSC or GDC (Scheme S1, ESI†). It is possible that atoms in the vicinity of the contact area with GDC phase exhibit a speciation that resembles that observed during the low oxygen concentration experiment. On the other hand, cobalt atoms near the LSC surface exposed to the gas phase would adopt a chemical speciation resembling that observed under synthetic air conditions. Hence, the improvement in the performance is not only because of more superficial active sites for the electrochemical reactions (favoured by the spherical shape of the GDC particles and the possible agglomeration of them, that keeps apart the LSC particles), and better connectivity between GDC spherical particles, but also because of the action of a breathing structure composed of Co^{2+}, Co^{3+} and Co^{4+} that facilitates anionic conduction to the LSC/GDC interface. The fast paths created by the better GDC connectivity complete the cycle, taking away the oxide species from the LSC phase, preventing the modification of the balance of cobalt species, the loss of oxygen vacancies, and active sites blocking by accumulation of adsorbed oxygen. This subtle relationship between GDC morphology, cobalt speciation and LSC electrochemical activity represents the key feature in the enhanced performance of LSC–GDC composite cathode with control of morphology. This hypothesis, however, needs to be tested by more specific experiments. Our work aims to highlight this relationship and encourage further investigations on this issue.

In consequence, the XANES results of our work substitutes the static picture with all cobalt atoms in a unique oxidation state (near +3), for a more dynamical model in which cobalt atoms reacts in a very specific way in response to changes in their surroundings (Scheme 1). The local cycling of cobalt atoms between +3 and +2/+4 oxidation states would be important for the $O_2(g)$ adsorption, O_2 dissociation and O reduction reactions, which were identified as the limiting process by our EIS study. This is in agreement with Tsvetkov *et al.*, who showed that oxygen vacancies play a secondary role in surface activity.[13] In addition, this local redox cycling (probably favoured by the electronic conduction of the material), along with the co-existence of the three cobalt cations (with their different ionic radius), would be beneficial for O^{2-} transport and transfer to the electrolyte phase. Some researchers have guessed this possibility through indirect methods, such as neutron powder diffraction.[63] Our results represent strong new evidence in favour of this picture.

In our case, EIS analysis suggests that the limiting processes in LSC–GDC composite cathodes take place on the surface of the LSC phase. Consequently, the existence of vacancies in bulk

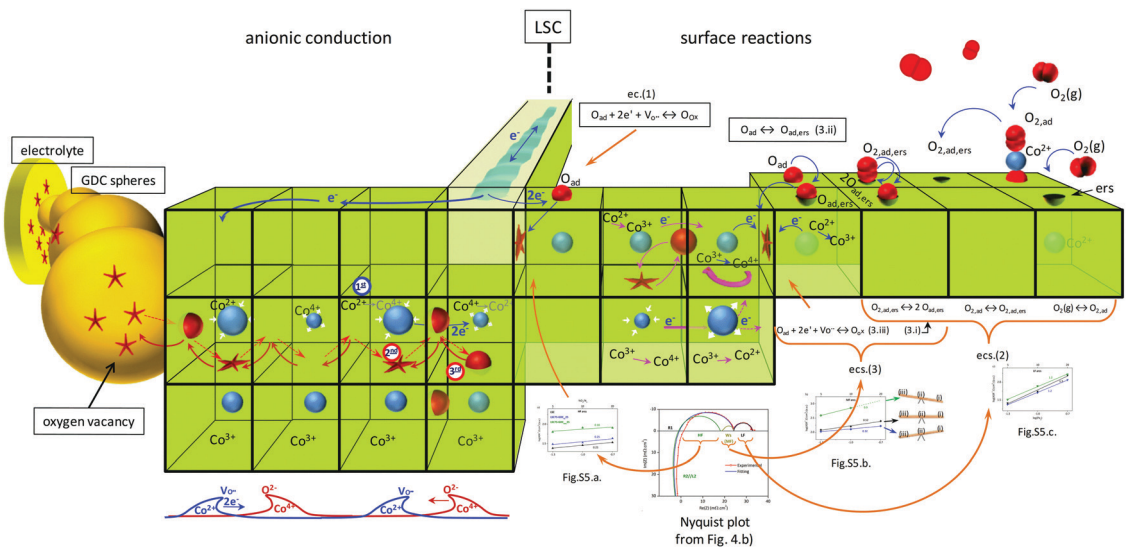

Scheme 1 Dynamical model for surface reactions and ionic conduction in LSC–GDC composite cathode based on the most important results found in this work. The ease of Co atoms for changing oxidation state, and disproportionation reaction, along with electronic conduction, are the key features to explain the LSC electrochemical properties. Better percolation of GDC spherical particles yield fast and efficient ionic paths from LSC to the electrolyte. This enhanced ionic flow depletes LSC surface electrochemical reaction sites and favours higher oxygen vacancy concentration, which lower the polarization losses of LSC–GDC composite cathode. "1st" indicates that charge transfer from Co^{2+} to Co^{4+} promotes vacancy conduction (2nd) in one way, and anionic conduction in the inverse direction (3rd). Inserted Fig. 4b and 5a–c, and eqn (1)–(3) are explained in terms of this schematic representation.

is not as important as the ease of cobalt atom for changing its oxidation state for the charge transfer process that takes place in the surface during oxygen reduction reaction or at the LSC/GDC interface. Our analysis cannot answer the question whether there is mass transport through the bulk of LSC phase, (mass transport would be fast enough so to not contribute significantly to the total ASR), or whether surface diffusion is favoured against bulk diffusion.

XANES and EIS analyses suggest that ease of cobalt atoms for changing its oxidation state along with surface oxygen vacancies are complementary key features that prompt oxygen surface diffusion.

Conclusions

In the present study, the electrochemical performance of nanostructured $La_{0.6}Sr_{0.4}CoO_{3-\delta}$–$Gd_{0.1}Ce_{0.9}O_{1.95}$ (LSC–GDC) composite cathodes for solid oxide fuel cell (SOFC) with different morphologies (LSC: nanostructured powders; GDC: nanostructured powders composed of particles with irregular shape or spherical particles) were experimentally evaluated.

The results obtained from complementary techniques suggest that the LSC phase in LSC–GDC composite cathodes is the active phase for $O_2(g)$ adsorption, diffusion, dissociation and reduction of atomic oxygen reactions, which seem to be the limiting processes. Composite cathodes made of 75 wt% LSC and 25 wt% GDC nanostructured spheres exhibited an enhanced performance as cathode in symmetrical cells using $Sm_{0.2}Ce_{0.8}O_{2-d}$ electrolytes. The decrease in the polarization resistance (ASR_{TOTAL} = 18.6(2) mΩ cm^2) was attributed to a faster depopulation of oxygen species on LSC surface, which kept active a high number of electrochemical reaction sites. This was favoured by the spherical shape of GDC particles, that provided good electrical contact and high speed paths for oxygen diffusion to the electrolyte (through a good percolation between GDC spherical particles), along with a minimum area of contact between LSC and GDC phases.

X-Ray absorption spectroscopy experiments proved to be a powerful probe to unveil the atomic origin of the electrochemical properties that cathode materials exhibit. Our study suggests that the electrochemical activity of LSC reported in this paper is based on the chemical properties exhibited by cobalt atoms. Novel information about cobalt's speciation in LSC under working-like conditions was presented in this work. The easiness with which cobalt atoms change their oxidation state according to the environment conditions of temperature and $O_2(g)$ concentration would be a key feature for adsorption of $O_2(g)$, diffusion and dissociation of O_2 and reduction of O atoms reactions, on one hand, and for O^{2-} transfer to the electrolyte phase, on the other. The spherical shape of the GDC particles may indirectly modify the chemical speciation of cobalt atoms, favouring the existence of Co^{2+} and Co^{4+} species and the local cycling of cobalt atoms between the three oxidation states. Importantly, this effect would contribute to the creation of a ''breathing structure'' in the LSC phase that favours the anionic conduction. A model describing the underlying mechanism is proposed.

In addition, and to the best of our knowledge, this is the first time that a transition from the regime of O^{2-} vacancy creation to disproportionation reaction in cobalt atoms was observed in nanostructured LSC upon heating, between 500 and 700 °C. After reaching a maximum oxygen vacancy concentration in the LSC lattice (associated to $\delta \approx 0.2$), the onset of the disproportionation reaction was interpreted as a mechanism that prevents nanostructured LSC from phase instability at higher temperatures and that would favour the electrochemical reactions between LSC and $O_2(g)$ on surface, and diminish the electronic resistance growth with increasing temperature. The coexistence of $Co^{2+,3+,4+}$ species would mechanically favour the oxide anion diffusion through the LSC lattice due to the different ionic radii, and the cycling in the local order of Co species between +2, +3 and +4 oxidation states would also dynamically drive the transport of O^{2-} anions.

As it was observed that for temperatures higher than 500 °C the amount of Co^{4+} starts to grow, exactly compensating the amount of Co^{2+}, it would be interesting to prove the hypothesis that the existence of Co^{4+} cations is the responsible for or, at least, contributes to, the electronic conduction in nanostructured LSC at high temperatures.

The effect of LSC particle's morphology (irregular nanopowders, nanotubes of different diameter, nanowires and others) on the electrochemical and thermomechanical properties of LSC–GDC composite cathodes represents an interesting issue to be explored in future works.

Conflicts of interest

There are no conflicts to declare.

Acknowledgements

This work has been supported by the Agency for Science and Technology (PICT 2016-1921, ANPCyT, Ministry of Science, Technology and Innovation, Argentine). This research used resources of the Brazilian Synchrotron Light Laboratory (LNLS), an open national facility operated by the Brazilian Centre for Research in Energy and Materials (CNPEM) for the Brazilian Ministry for Science, Technology, Innovations and Communications (MCTIC). The D08B-XAFS2 beam line staff, Fávio Sambello, and Simone Baú Betim and Tamiris Bouças Piva from the Laboratory of Chemistry (LQU) are acknowledged for the assistance during the experiments. Dr D. Vega (CAC-CNEA, Argentina) and the X-Ray National System (SNRX, MINCYT, Argentina) for the XRD facilities. The authors are members of CIC-CONICET, Argentina.

Notes and references

1 B. C. H. Steele and A. Heinzel, *Nature*, 2001, **414**, 345–352.
2 Z. Gao, L. V. Mogni, E. C. Miller, J. G. Railsback and S. A. Barnett, *Energy Environ. Sci.*, 2016, **9**, 1602–1644.

3 S. J. Skinner, *Int. J. Inorg. Mater.*, 2001, **3**, 113–121.
4 S. B. Adler, *Solid State Ionics*, 1998, **111**, 125–134.
5 H. Uchida, S. Arisaka and M. Watanabe, *Solid State Ionics*, 2000, **135**, 347–351.
6 D. Prieur, W. Bonani, K. Popa, O. Walter, K. W. Kriegsman, M. H. Engelhard, X. Guo, R. Eloirdi, T. Gouder, A. Beck, T. Vitova, A. C. Scheinost, K. Kvashnina and P. Martin, *Inorg. Chem.*, 2020, **59**, 5760–5767.
7 L. M. Acuña, J. Peña-Martínez, D. Marrero-López, R. O. Fuentes, P. Nuñez and D. G. Lamas, *J. Power Sources*, 2011, **196**, 9276–9283.
8 L. M. Acuña, F. F. Muñoz and R. O. Fuentes, *J. Phys. Chem. C*, 2016, **120**, 20387–20399.
9 J. Sacanell, A. G. Leyva, M. G. Bellino and D. G. Lamas, *J. Power Sources*, 2010, **195**, 1786–1792.
10 M. G. Bellino, J. G. Sacanell, D. G. Lamas, A. G. Leyva and N. E. Walsöe De Reca, *J. Am. Chem. Soc.*, 2007, **129**, 3066–3067.
11 L. Dieterle, P. Bockstaller, D. Gerthsen, J. Hayd, E. Ivers-Tiffée and U. Guntow, *Adv. Energy Mater.*, 2011, **1**, 249–258.
12 K. Develos-Bagarinao, R. A. Budiman, S. S. Liu, T. Ishiyama, H. Kishimoto and K. Yamaji, *J. Power Sources*, 2020, **453**, 227894.
13 N. Tsvetkov, Q. Lu, L. Sun, E. J. Crumlin and B. Yildiz, *Nat. Mater.*, 2016, **15**, 1010–1016.
14 S. Wang, J. Yoon, G. Kim, D. Huang, H. Wang and A. J. Jacobson, *Chem. Mater.*, 2010, **22**, 776–782.
15 L. Dos Santos-Gómez, S. Sanna, P. Norby, N. Pryds, E. R. Losilla, D. Marrero-López and V. Esposito, *Nanoscale*, 2019, **11**, 2916–2924.
16 A. Heel, P. Holtappels and T. Graule, *J. Power Sources*, 2010, **195**, 6709–6718.
17 S. Wang, T. Kobayashi, M. Dokiya and T. Hashimoto, *J. Electrochem. Soc.*, 2000, **147**, 3606.
18 Y. Tao, J. Shao, W. G. Wang and J. Wang, *Fuel Cells*, 2009, **9**, 679–683.
19 S. Park, S. Choi, J. Shin and G. Kim, *Electrochim. Acta*, 2014, **125**, 683–690.
20 F. Wei, H. Cao and X. Chen, *J. Mater. Sci.*, 2016, **51**, 2160–2167.
21 C. Benel, A. J. Darbandi, R. Djenadic, A. Evans, R. Tölke, M. Prestat and H. Hahn, *J. Power Sources*, 2013, **229**, 258–264.
22 H. Yokokawa, N. Sakai, T. Horita, K. Yamaji, M. E. Brito and H. Kishimoto, *J. Alloys Compd.*, 2008, **452**, 41–47.
23 R. Knibbe, J. Hjelm, M. Menon, N. Pryds, M. Søgaard, H. J. Wang and K. Neufeld, *J. Am. Ceram. Soc.*, 2010, **93**, 2877–2883.
24 M. Shiono, K. Kobayashi, T. L. Nguyen, K. Hosoda, T. Kato, K. Ota and M. Dokiya, *Solid State Ionics*, 2004, **170**, 1–7.
25 S. B. Adler, X. Y. Chen and J. R. Wilson, *J. Catal.*, 2007, **245**, 91–109.
26 Y. C. Chen, M. Yashima, T. Ohta, K. Ohoyama and S. Yamamoto, *J. Phys. Chem. C*, 2012, **116**, 5246–5254.
27 Y. Orikasa, T. Ina, T. Nakao, A. Mineshige, K. Amezawa, M. Oishi, H. Arai, Z. Ogumi and Y. Uchimoto, *J. Phys. Chem. C*, 2011, **115**, 16433–16438.
28 M. H. R. Lankhorst, H. J. M. Bouwmeester and H. Verweij, *J. Solid State Chem.*, 1997, **133**, 555–567.
29 A. N. Petrov, V. A. Cherepanov, O. F. Kononchuk and L. Y. Gavrilova, *J. Solid State Chem.*, 1990, **87**, 69–76.
30 J. L. Hueso, J. P. Holgado, R. Pereñíguez, V. M. Gonzalez-Delacruz and A. Caballero, *Mater. Chem. Phys.*, 2015, **151**, 29–33.
31 P. Hjalmarsson, M. Søgaard, A. Hagen and M. Mogensen, *Solid State Ionics*, 2008, **179**, 636–646.
32 V. V. Efimov, E. Efimova, D. Karpinsky, D. I. Kochubey, V. Kriventsov, A. Kuzmin, S. Molodtsov, V. Sikolenko, J. Purans, S. Tiutiunnikov, I. O. Troyanchuk, A. N. Shmakov and D. Vyalikh, *Nucl. Instrum. Methods Phys. Res., Sect. A*, 2007, **575**, 176–179.
33 O. Haas, C. Ludwig, U. Bergmann, R. N. Singh, A. Braun and T. Graule, *J. Solid State Chem.*, 2011, **184**, 3163–3171.
34 V. Sikolenko, A. Sazonov, V. Efimov, V. Krivencov, N. Darowski and D. Vyalikh, *J. Magn. Magn. Mater.*, 2007, **310**, 2006–2008.
35 T. Itoh, M. Inukai, N. Kitamura, N. Ishida, Y. Idemoto and T. Yamamoto, *J. Mater. Chem. A*, 2015, **3**, 6943–6953.
36 Y. Takeda, R. Kanno, M. Noda, Y. Tomida and O. Yamamoto, *J. Electrochem. Soc.*, 2019, **134**, 2656–2661.
37 D. Baskar and S. B. Adler, *ECS Trans.*, 2019, **7**, 1279–1286.
38 R. O. Fuentes and R. T. Baker, *J. Power Sources*, 2009, **186**, 268–277.
39 F. F. Muñoz, L. M. Acuña, C. A. Albornoz, A. G. Leyva, R. T. Baker and R. O. Fuentes, *Nanoscale*, 2015, **7**, 271–281.
40 H. Taguchi, S. Yamada, M. Nagao, Y. Ichikawa and K. Tabata, *Mater. Res. Bull.*, 2002, **37**, 69–76.
41 V. G. Milt, M. A. Ulla and E. E. Miró, *Appl. Catal. B: Environ.*, 2005, **57**, 13–21.
42 H. Kozuka, H. Yamada, T. Hishida, K. Yamagiwa, K. Ohbayashi and K. Koumoto, *J. Mater. Chem.*, 2012, **22**, 20217–20222.
43 S. J. A. Figueroa, J. C. Mauricio, J. Murari, D. B. Beniz, J. R. Piton, H. H. Slepicka, M. F. De Sousa, A. M. Espíndola and A. P. S. Levinsky, *J. Phys.: Conf. Ser.*, 2016, **712**, 1–6.
44 S. Calvin, *XAFS for Everyone*, CRC Press, 2013.
45 T. Ressler, *J. Synchrotron Radiat.*, 1998, **5**, 118–122.
46 O. Gwon, S. Yoo, J. Shin and G. Kim, *Int. J. Hydrogen Energy*, 2014, **39**, 20806–20811.
47 A. Jun, J. Kim, J. Shin and G. Kim, *ChemElectroChem*, 2016, **3**, 511–530.
48 A. N. Petrov, O. F. Kononchuk, A. V. Andreev, V. A. Cherepanov and P. Kofstad, *Solid State Ionics*, 1995, **80**, 189–199.
49 N. M. L. N. P. Closset, R. H. E. Van Doorn and H. Kruidhof, *Powder Diffr.*, 1996, **11**, 31–34.
50 Y. T. Kim and N. Shikazono, *Solid State Ionics*, 2017, **309**, 77–85.
51 J. R. Macdonald and D. R. Franceschetti, *J. Chem. Phys.*, 1978, **68**, 1614–1637.
52 J. M. Lattimer and M. Prakash, *Science*, 2004, **304**, 536–542.
53 A. Ringuedé and J. Fouletier, *Solid State Ionics*, 2001, **139**, 167–177.

54 V. A. Sadykov, S. N. Pavlova, V. S. Kharlamova, V. S. Muzykantov, N. F. Uvarov, Y. S. Okhupin, A. V. Ishchenko, A. S. Bobin, N. V. Mezentseva, G. M. Alikina, A. I. Lukashevich, T. A. Krieger, T. V. Larina, N. N. Bulgakov, V. M. Tapilin, V. D. Belyaev, E. M. Sadovskaya, A. I. Boronin, V. A. Sobyanin, A. F. Bobrenok, A. L. Smirnova, O. L. Smorygo and J. A. Kilner, in *Perovskites: Structure, Properties and Uses*, ed. M. Borowski, Nova Science Publishers, Inc., 2010, pp. 67–178.
55 A. Mineshige, M. Kobune, S. Fujii, Z. Ogumi and M. Inaba, *J. Solid State Chem.*, 1999, **381**, 374–381.
56 M. a Senaris-Rodriguez and J. B. Goodenough, *J. Solid State Chem.*, 1995, **118**, 323–336.
57 O. Toulemonde, N. N'Guyen, F. Studer and A. Traverse, *J. Solid State Chem.*, 2001, **158**, 208–217.
58 M. Abbate, J. C. Fuggle, A. Fujimori, L. H. Tjeng, C. T. Chen, R. Potze, G. A. Sawatzky, H. Eisaki and S. Uchida, *Phys. Rev. B: Condens. Matter Mater. Phys.*, 1993, **47**, 16124–16130.
59 B. Raveau and M. M. Seikh, *Cobalt Oxides*, 2012, 3–70.
60 M. Søgaard, P. V. Hendriksen, M. Mogensen, F. W. Poulsen and E. Skou, *Solid State Ionics*, 2006, **177**, 3285–3296.
61 Y. Tokura and N. Nagaosa, *Science*, 2000, **288**, 462 LP–468.
62 H. Kozuka, H. Yamada, T. Hishida, K. Yamagiwa, K. Ohbayashi and K. Koumoto, *J. Mater. Chem.*, 2012, **22**, 20217–20222.
63 Y. Gong, C. Sun, Q. A. Huang, J. A. Alonso, M. T. Fernández-Díaz and L. Chen, *Inorg. Chem.*, 2016, **55**, 3091–3097.